ENHANCED PHOTOCATALYTIC ACTIVITY OF C-DOPED CeO_2 NANOPARTICLES UNDER VISIBLE LIGHT IRRADIATION FOR DEGRADATION OF METHYLENE BLUE**

Ta Quoc Tuan [1*], Pham Van Huan [1], Bui Thi Hoan [2], Hoang Nhu Van [3,4], Do Duy Hung [5], Nguyen Ngoc Trung [5], Hoang An Nghia [6], Nguyen Dinh Hoa [6], Phuong Dinh Tam [3,4], Vuong-Hung Pham [1*]

[1] International Training Institute for Materials Science (ITIMS), Hanoi University of Science and Technology (HUST), Hanoi, Vietnam; e-mail: vuong.phamhung@hust.edu.vn, tuan.taquoc@hust.edu.vn
[2] Faculty of Electrical – Electronics Engineering, Thuyloi University, Hanoi, Vietnam
[3] Faculty of Materials Science and Engineering, Phenikaa University, Yen Nghia, Vietnam
[4] Phenikaa Research and Technology Institute, A&A Green Phoenix Group, Hanoi, Vietnam
[5] School of Engineering Physics, Hanoi University of Science and Technology (HUST), Hanoi, Vietnam
[6] Administrative Office, Hanoi University of Science and Technology (HUST), Hanoi, Vietnam

C-doped CeO_2 nanoparticles were synthesized by hydrothermal method using glucose as carbon source. The structure of the C-doped CeO_2 nanoparticles was controlled by the concentration of the glucose precursor. The structure and properties of the C-doped CeO_2 nanoparticles were characterized by X-ray diffraction and UV-Vis diffuse reflectance spectroscopy. Microscopic morphology of nanoparticles was characterized by transmission electron microscopy. Photocatalytic activity was assessed by considering the degradation of methylene blue under visible light irradiation. Results show that C-doping significantly improves the photocatalytic activity of CeO_2 nanoparticles because of the combination of extending radiation absorption in visible light and the efficient separation of electron-hole pairs. These findings suggest that the present method is useful for controlling the microstructure and dye degradation properties of C-doped CeO_2 nanoparticles, which is particularly important for catalyst engineering.

Keywords: *CeO_2, catalyst, nanoparticles, UV-Vis-spectroscopy.*

УСИЛЕНИЕ ФОТОКАТАЛИТИЧЕСКОЙ АКТИВНОСТИ НАНОЧАСТИЦ CeO_2, ЛЕГИРОВАННЫХ УГЛЕРОДОМ, ПРИ ОБЛУЧЕНИИ ВИДИМЫМ СВЕТОМ ДЛЯ ДЕГРАДАЦИИ МЕТИЛЕНОВОГО СИНЕГО

T. Q. Tuan [1*], P. V. Huan [1], B. T. Hoan [2], H. N. Van [3,4], D. D. Hung [5], N. N. Trung [5], H. A. Nghia [6], N. D. Hoa [6], P. D. Tam [3,4], V.-H. Pham [1*]

УДК 543.42:620.3

[1] Международный учебный институт материаловедения Ханойского университета науки и технологий, Ханой, Вьетнам; e-mail: vuong.phamhung@hust.edu.vn, tuan.taquoc@hust.edu.vn
[2] Университет Туйлой, Ханой, Вьетнам
[3] Университет Финикаа, Йен Нгиа, Вьетнам
[4] Научно-исследовательский технологический институт Феникаа, A&A Green Phoenix Group, Ханой, Вьетнам
[5] Школа инженерной физики Ханойского университета науки и технологий, Ханой, Вьетнам
[6] Административный офис Ханойского университета науки и технологий, Ханой, Вьетнам

(Поступила 13 сентября 2022)

Наночастицы CeO_2, легированные углеродом, синтезированы гидротермальным методом с использованием глюкозы в качестве источника углерода. Структура полученных наночастиц контро-

** Full text is published in JAS V. 90, No. 5 (http://springer.com/journal/10812) and in electronic version of ZhPS V. 90, No. 5 (http://www.elibrary.ru/title_about.asp?id=7318; sales@elibrary.ru).

лировалась концентрацией предшественника глюкозы, и свойства исследованы методами рентгеновской дифракции и спектроскопии диффузного отражения в УФ-видимой области. Морфология наночастиц охарактеризована с помощью просвечивающей электронной микроскопии. Фотокаталитическая активность оценена по разложению метиленового синего под действием видимого света. Показано, что легирование углеродом значительно усиливает фотокаталитическую активность наночастиц CeO_2 из-за увеличения поглощения излучения в видимом диапазоне в сочетании с эффективным разделением электронно-дырочных пар. Метод можно применять для контроля микроструктуры и свойств разложения красителя с помощью наночастиц CeO_2, легированных углеродом, что особенно важно для разработки катализаторов.

Ключевые слова: *CeO_2, катализатор, наночастица, УФ-видимая спектроскопия.*

Introduction. Wastewater pollution is a matter of concern worldwide, especially in water sources contaminated by persistent organic compounds, such as those containing stable benzene rings, which are not degraded by living organisms, whether aerobic or anaerobic. The emission sources of these organic pollutants can be factories where plant protection drugs are produced and textiles are dyed [1]. A variety of wastewater treatment solutions for organic pollutants have been studied through advanced oxidation, nanophotocatalysts, ceramic nanofiltration membranes, photocatalytic oxidation, and nanophotocatalysts coupled with ceramic nanofiltration membranes [2]. Photocatalysis has attracted intense attention because it uses solar radiation to excite electrons in semiconductors, creating electron-hole pairs that combine with water to form strong oxidizing radicals. This involves an advanced oxidation processes similar to that of Fenton's reagent.

Many semiconductors have been studied as photocatalysts such as TiO_2, ZrO_2, CeO_2, and C_3N_4 [3–6]. Among them, cerium oxide (CeO_2) is a promising material. CeO_2 has a wide range of applications in many fields, including photocatalysts, UV absorbers, ceramics, inorganic membranes, sensors, solar converters, and automotive catalytic converters [5, 7–9]. Moreover, CeO_2 is chemically stable and exists in the form of a divalent state Ce^{3+}/Ce^{4+} redox pair, which benefits the formation of oxygen vacancies, thereby increasing the photocatalytic efficiency of the material [10]. However, like conventional photocatalysts, CeO_2 has a large band gap E_g (2.8–3.1 eV) and only absorbs ultraviolet radiation. The photocatalytic performance of CeO_2 is low and still has many disadvantages such as fast hole-electron recombination rate and low specific surface area. To improve the photocatalytic performance of CeO_2, many solutions have been proposed, including creating hierarchical structures with other oxides that have a smaller band gap, and doping in CeO_2 with metal ions such as Fe^{3+}, Co^{3+}, and Y^{3+} ions [11–13]. The ions doped into CeO_2 reduce the band gap, extending the absorption region of CeO_2 toward visible light. On the other hand, impure ions also reduce the recombination of electrons and holes, thereby increasing the photocatalytic efficiency.

Another aspect is the doping of semiconductor oxides with nonmetals such as N doped into TiO_2 and C doped into TiO_2, which also enhances the photocatalytic efficiency [14, 15]. Hydrothermal method is effective in synthesizing CeO_2 nanoparticles [16, 17]; however, to the best of our knowledge, no studies have been published on the effect of carbon (C) doping into CeO_2 nanoparticles on the microstructure and photocatalytic performance. We used the hydrothermal method to synthesize C-doped CeO_2 nanoparticles from precursors of glucose and cerium nitrate. This method is simple and cost-effective for the synthesis of C-doped CeO_2 nanoparticles with effective photodegradation of methylene blue (MB) under visible light irradiation.

Experimental. C-doped CeO_2 nanoparticles were synthesized via a hydrothermal method as follows: an aqueous solution containing 0.15 M cerium nitrate hexahydrate $Ce(NO_3)_3 \cdot 6H_2O$ (99.9% purity, Aldrich) was prepared. Different aqueous solutions of glucose ($C_6H_{12}O_6$, 99.9% purity, Merck) were added to the aforementioned solution. The concentration of the glucose solution was based on the designed C concentrations in CeO_2 ($Ce_{1-x}C_xO_2$), which are x = 0, 0.05, 0.1, and 0.2, and 0–20 mol.% C. The solutions were stirred for 0.5 h by a magnetic stirrer at room temperature and then precipitated using 10 wt.% ammonia solution with a controlled pH value of 10. The mixture was transferred into a 100 mL Teflon-lined autoclave, then the autoclave was covered and maintained at 200°C for 12 h. The resulting precipitates were washed twice with deionized water and ethanol and then dried at 100°C for 6 h.

The crystal structures of C-doped CeO_2 nanoparticles were characterized by X-ray diffraction (XRD, D8 Advance, Bruker, Germany). The C-doped CeO_2 microstructure was determined by TEM (JEOL, JEM 1010, JEOL, Tokyo, Japan). The elemental composition and chemical bonding of C-doped CeO_2 were determined by FE-SEM (JEOL, JSM−7600F, JEOL, Tokyo, Japan) and FTIR (PerkinElmer Spectrum

BX spectrometer, Waltham, MA, USA). The band gap was determined from UV-Vis diffuse reflectance spectroscopy (Jasco V-760 UV-Visible spectrophotometer, Tokyo, Japan).

The photocatalytic efficiency in methylene blue (MB) degradation was investigated under irradiation using a 100 W Xenon lamp as simulated sunlight. Then, 20 mg of CeO_2 or C-doped CeO_2 nanoparticles were added to 30 mL of 10 mg/L MB solution (10 ppm). The solution was stirred for 30 min in the dark light before Xenon irradiation. After different light irradiation times, the suspensions were collected and then centrifuged (4500 rpm, 5 min) to remove the photocatalyst particles. The MB concentrations were monitored using a UV-Vis spectrophotometer (Cary 500 spectrometer, Agilent, Santa Clara, CA, USA).

Results and discussion. Figure 1 shows a powder X-ray diffraction pattern of the C-doped CeO_2 nanoparticles with different C doping concentrations. All samples show well-indexed peak diffraction intensity with the cubic fluorinated crystalline phase of the CeO_2 (JCPDS card no. 34-0394). The 2θ positions at approximately 28.5, 33.1, 47.5, 56.4, and 59.1° angular diffraction peaks are assigned to the diffraction planes (111), (200), (220), (311), and (222) of the cubic CeO_2 phase, respectively.

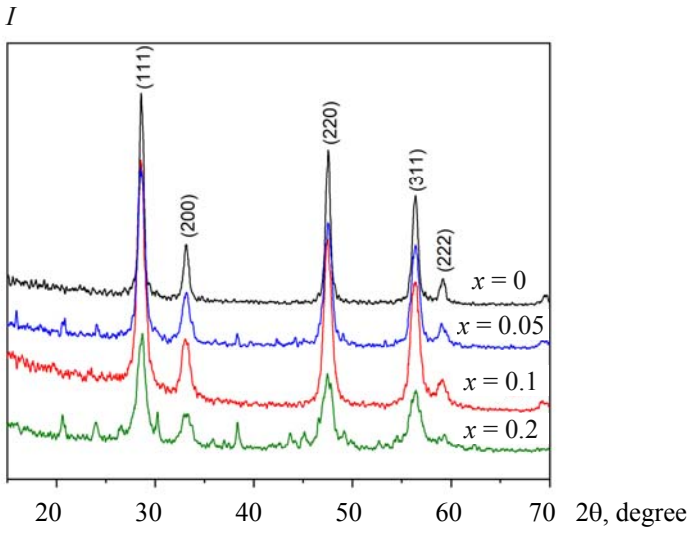

Fig. 1. XRD patterns of the $Ce_{1-x}C_xO_2$ nanoparticles, x = 0–0.2.

The full-width half maximum (FWHM) of the peaks tended to increase as the C-doping concentration increased, which allowed us to predict that the crystal size of the C-doped CeO_2 nanoparticles would decrease. To confirm the influence of C-doping concentration on the crystal size change, we calculated the crystal grain size by applying the Debye–Scherrer (D-S) and Williamson–Hall (W-H) methods [18]. The D-S equation is

$$D = k\lambda/\beta\cos\theta. \quad (1)$$

The W-H equation can be expressed as

$$\beta\cos\theta = \varepsilon(4\sin\theta) + \lambda/D, \quad (2)$$

where θ, D, ε, and β are Bragg angle, grain size, microscopic strain, and FWHM, respectively. K is a constant that depends on the shape of the particle (0.90) and the wavelength of the CuK_α radiation (λ = 1.542 Å).

Figure 2 shows a W-H plot depicting the effect of C concentration on the lattice defects of the CeO_2 nanoparticles. The X-axis is the value of 4sinθ and the Y-axis is the value of βcosθ. The function graph has the form $y = ax + b$. Linear fitting is done to provide the parameters, where the slope (a = ε) describes the strain (ε) and (b = λ/D) with respect to the crystal size (D), microstrain (ε), stacking fault (SF), and dislocation density (δ) that were calculated using the following formulas:

$$\delta = 1/D^2, \quad (3)$$

$$\mathrm{SF} = \left[\frac{2\pi^2}{45(3\tan\theta)^{1/2}}\right]\beta. \quad (4)$$

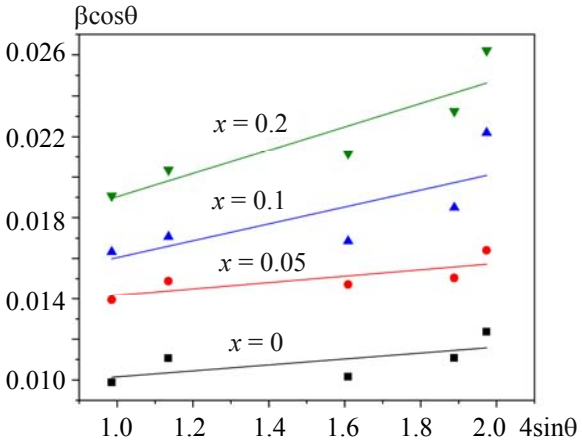

Fig. 2. W–H plots of the $Ce_{1-x}C_xO_2$ nanoparticles, x = 0–0.2.

The results are shown in Table 1. As the C-doping concentration increases, the crystal size tends to decrease and the lattice strain, dislocation density, and stacking fault value also increase. These results can be attributed to the effect of C-doping resulting in crystal deformation; thus, the crystal growth decreases.

The crystal size of the $Ce_{1-x}C_xO_2$ nanoparticles in W-H ranges were in the range of 11.6–17.7 nm. These values were larger than those calculated by the D-S equation (Table 1). The reason for the difference in values is that the strain component in the Scherrer formula is assumed to be 0. The W-H method uses all strain components. We proceed to refine the structure using the Rietveld method to estimate the cell volume and lattice strain of the $Ce_{1-x}C_xO_2$ (x = 0, 0.05, 0.1, 0.2). Analysis was performed using the FullProf program. The pseudo-Voigt function was used to adjust parameters such as one zero shifting, one scale factor, three cell parameters, four backgrounds, five shapes and widths of the peaks, and two asymmetric factors; other parameters were used as shown in [19].

Figure 3 shows the Rietveld refinement results of the $Ce_{1-x}C_xO_2$ nanoparticles. The results showed a good agreement between the experimental intensity and calculated XRD intensity. The Rietveld-refined structural parameters of the $Ce_{1-x}C_xO_2$ nanoparticles (x = 0, 0.05, 0.1, 0.2) are presented in Table 2.

TABLE 1. Estimated Crystallite Size (D), Strain (ε), Stacking Fault (SF), and Dislocation Density (Δ) of $Ce_{1-x}C_xO_2$ Nanoparticles, x = 0–0.2

Samples	Crystallite, size, nm		Strain×(ε)10^{-3}	SF×10^{-2}	Δ (10^{15} lin/m^2)
	Scherrer's	W-H			
x = 0	14.1	17.7	1.46	2.55	5.03
x = 0.05	9.9	12.9	1.57	3.61	10.20
x = 0.15	8.5	12.2	4.14	4.22	13.84
x = 0.20	7.2	11.6	5.75	4.94	19.29

TABLE 2. Rietveld Refined Structural Parameters of $Ce_{1-x}C_xO_2$ Nanoparticles, x = 0–0.2

Parameters	CeO_2	x = 0.05	x = 0.1	x = 0.2
Crystal system	Cubic	Cubic	Cubic	Cubic
Space group	$Fm\bar{3}m$	$Fm\bar{3}m$	$Fm\bar{3}m$	$Fm\bar{3}m$
Lattice parameter				
$a = b = c$, Å	5.451	5.467	5.488	5.468
Unit cell volume/formular unit, Å^3	161.97	163.40	165.29	163.49
α = β = γ, degree	90	90	90	90
R_P	8.182	11.88	8.151	8.608
R_{WP}	7.022	8.900	3.519	7.942
R_{exp}	2.831	3.759	7.730	4.696
χ^2	6.15	5.61	0.21	2.86

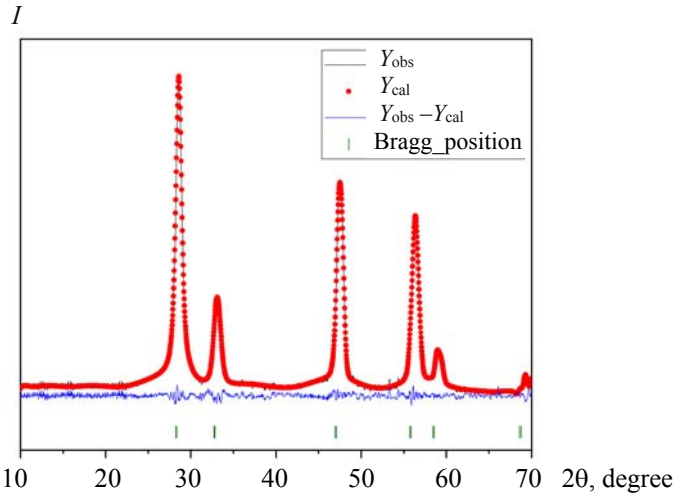

Fig. 3. Rietveld refinement of the $Ce_{1-x}C_xO_2$ nanoparticles, $x = 0.1$.

The C-doped CeO_2 and the CeO_2 nanoparticles exist in cubic form. The unit cell size of the C-doped CeO_2 nanoparticles does not change significantly as the C-doping concentration increases. The radius of the coordination number of C ion 4 (0.29 Å) is much smaller than that of the radius of Ce^{4+} ion coordination number 8 (1.1 Å). Thus, carbon atoms can only partially replace the Ce^{4+} sites and the remaining carbon atoms can enter interstitial sites or surround the CeO_2 particle.

The microstructural morphology of the C-doped CeO_2 and the CeO_2 nanoparticles was examined by TEM as shown in Figs. 4a–d. The undoped CeO_2 nanoparticles show a short nanorod structure with a length of ~18 nm and a diameter of ~12 nm (Fig. 4a). When the amount of C was doped to 5 mol.%, the samples still displayed a short rod-like morphology with a length of 22 nm and a diameter of ~12 nm (Fig. 4b). On the other hand, when the glucose was increased to 10 mol.% C concentration, the specimen had a rounded morphology with a diameter of ~14 nm (Fig. 4c). The circular morphology of this particle was more impressive with a diameter of ~12 nm when a higher concentration of C-doping (20 mol.%) was used (Fig. 4d). The significant morphological difference in the variation of C-doping concentrations suggests that C plays an important role in controlling growth and crystallization. The morphological change of the C-doped CeO_2 nanoparticles by increasing glucose concentration could be explained by the fact that glucose altered the growth of CeO_2 crystals during growth, which caused the crystals to grow into isotropic CeO_2. To better understand the growth of the crystal planes, we conduct high-resolution TEM (HR–TEM) image analysis of the C-doped CeO_2 nanoparticles with 10 mol.% C concentration, as shown in Figs. 4e,f. The figure shows that the plane (111) exists with a lattice distance of 3.125 Å.

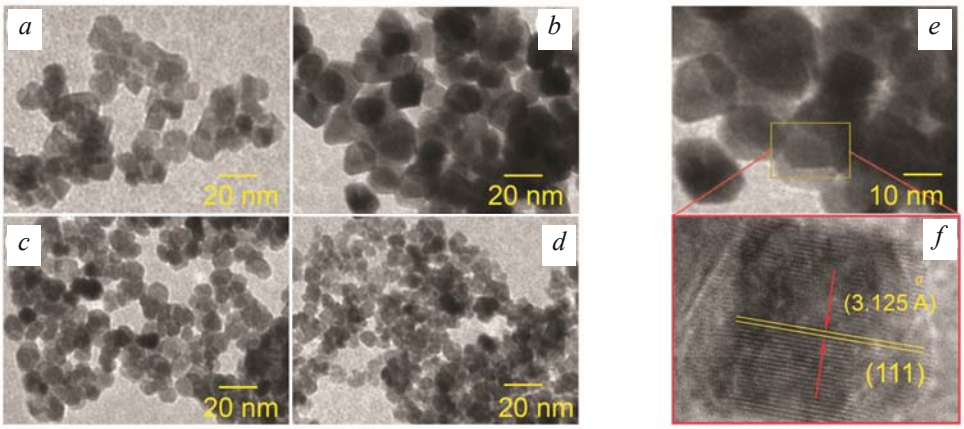

Fig. 4. TEM images of the $Ce_{1-x}C_xO_2$ nanoparticles: $x = 0$ (a), 0.05 (b), 0.1 (c), and 0.2 (d); (e) HR-TEM images of $Ce_{1-x}C_xO_2$ nanoparticles, $x = 0.1$; (f) zoom HR-TEM $Ce_{1-x}C_xO_2$ nanoparticles, $x = 0.1$.

The CeO_2 fluorite structure possesses three low-index planes, namely, very stable plane (111), less stable plane (110), and higher energy plane (001) [20, 21]. In general, the crystal growth tends to minimize the total surface energy, and CeO_2 crystals grow in the (001) direction to form a short rod structure with C-doping using glucose. However, when a certain amount of glucose is added to the solution, the glucose anion with the -CO and -OH groups is absorbed on the positively charged Ce^{4+} (001) plane. Then, it inhibits the contact between the growth and crystal surface (001) of the increased units, which can lead to the formation of rounder nanoparticles with smaller diameters. These results are also in good agreement with those of crystal size calculation by X-ray diffraction.

The representative chemical composition and chemical bonding of the C-doped CeO_2 nanoparticles were characterized by EDS and FTIR. Figure 5a shows the typical FTIR spectra of the C-doped and undoped CeO_2 nanoparticles. The FTIR spectra illustrate the characterization of Ce-O-Ce and Ce-O at ~700 and 1150 cm^{-1} bound in CeO_2 [22, 23]. The wide band at approximately 3449 cm^{-1} and the absorption band at around 1634 and 1381 cm^{-1} were assigned to the OH- ions and the O-H oscillation of the H_2O molecule absorbed in the nanoparticle [24]. Interestingly, the banding occurrence at ~533 and 1786–1821 cm^{-1} is related to the C-O and C=O bands, respectively, and is therefore considered a specific feature of C doped with CeO_2 [25]. EDS analysis of C-doped CeO_2 nanoparticles mounted on a Si conductive wafer showed that peaks corresponding to carbon were observed (Fig. 5b), indicating the presence of carbon in the CeO_2 nanoparticles. In addition, the calculated atomic concentration of C in the CeO_2 nanoparticles is ~17.1%, which indicates that these structures are the C-doped CeO_2 nanoparticle.

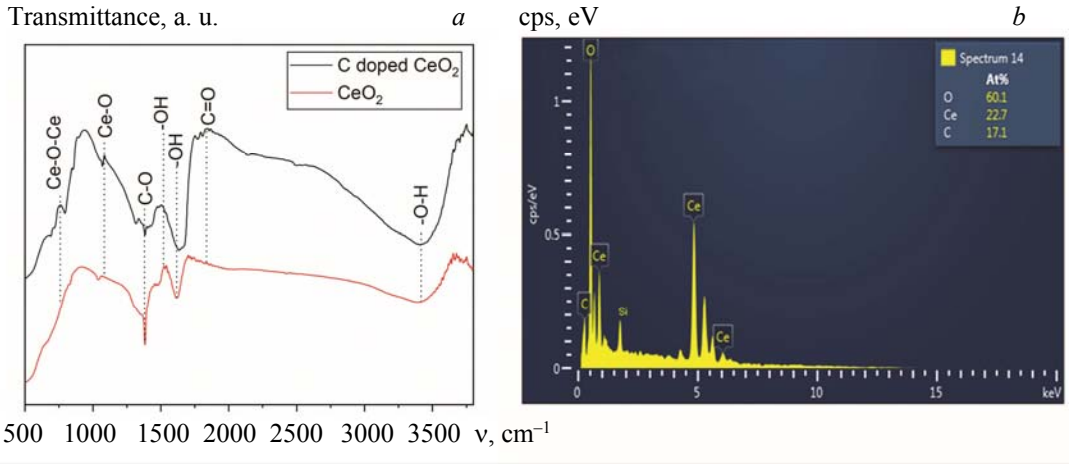

Fig. 5. (a) FT-IR spectra of the $Ce_{1-x}C_xO_2$ nanoparticles, $x = 0$ and 0.1; (b) EDS of the $Ce_{1-x}C_xO_2$ nanoparticles, $x = 0.1$.

Figure 6 shows the optical properties of the C-doped CeO_2. The CeO_2 nanoparticles were investigated using UV-Vis diffuse reflectance spectroscopy. The pure CeO_2 exhibits strong absorption in the UV region with an absorption margin around 388 nm, suggesting that CeO_2 can only be excited by UV light. The C-doped CeO_2 nanoparticles display a wide absorption region from UV to visible light with an absorption edge of approximately 550 nm. As the C-doping concentration gradually increased, a shift to the visible absorption region occurred, and the same red shift for other C-doped oxides, such as carbon-doped TiO_2, was also observed [15].

We calculated the band gap of the C-doped CeO_2 and the CeO_2 nanoparticles according to Tauc's equation [26]:

$$\alpha h\nu = A(h\nu - E_g)^n, \quad (5)$$

where α is a constant; A, h, n, and E_g are the absorption coefficient, Planck constant, light frequency, and band gap, respectively. The power index n depends on the type of electronic transition, i.e., n is 1/2 for materials with a direct band gap and $n = 2$ for materials with an indirect bandgap. $n = 2$ was chosen in this study because CeO_2 is an indirect conversion material. Inset in Fig. 6 shows a graph of $(\alpha h\nu)^2$ versus energy ($h\nu$). For the C-doped CeO_2 nanoparticles $E_g = 3.2$ ($x = 0$), 3.1 ($x = 0.05$), 2.9 ($x = 0.1$), and 2.6 eV ($x = 0.15$).

The band gap of the CeO_2 was reduced from 3.2 to 2.6 eV with the increase of C concentration from 0 to 15 mol.%. This narrowing of the band gap is due to C doping, through which the C acceptor creates an energy level near the valence band edge, forming bands located in the conduction band.

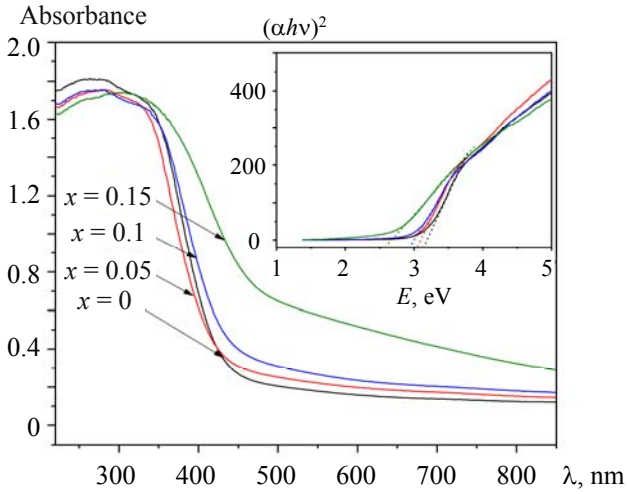

Fig. 6. UV-Vis diffuse reflectance spectrum and Tauc's plot for the band gap calculation of the $Ce_{1-x}C_xO_2$ nanoparticles, x = 0–0.15.

Figure 7 shows the time-dependent UV-Vis spectrum of MB degradation in the presence of the C-doped CeO_2 catalyst with 10 mol.% C concentration under visible light irradiation. The intensity of the characteristic absorption peak of the MB solution decreases with the time of visible light irradiation. These results were also in good agreement with the optical image showing the degradation of MB as a function of irradiation time (inset of Fig. 7). The MB degradation reached nearly 94.6% after 180 min of visible light irradiation. Thus, the C-doped CeO_2 nanoparticle is an efficient photocatalyst for the MB degradation.

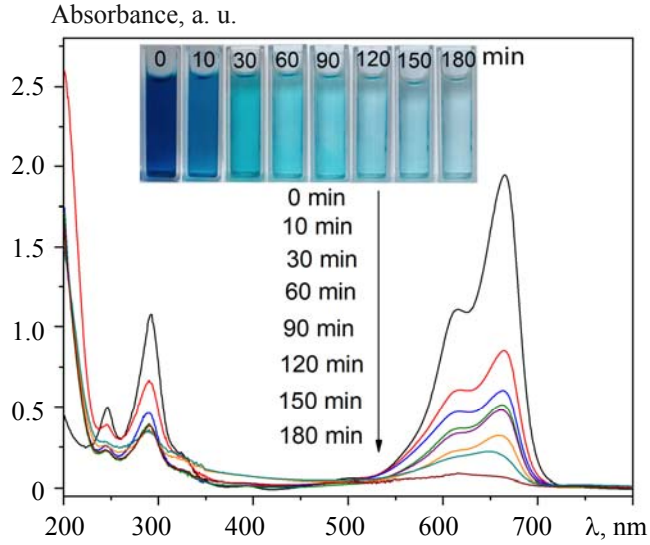

Fig. 7. Photodegradation of MB under visible light irradiation with different times in the presence of the $Ce_{1-x}C_xO_2$ nanoparticles, x = 0.1.

We further studied the effect of the C-doping concentration on MB degradation efficiency in the presence of the C-doped CeO_2 nanoparticles with 0–20 mol% C under visible light irradiation. Figure 8 shows that the MB degradation efficiency increases gradually as the C-doping concentration increases, reaching the maximum efficiency at 10 mol.% C. MB degradation processes displayed first-order kinetics by plotting $\ln(C/C_0)$ versus irradiation time, t. The apparent response rate constant (k_{app}) was calculated from the slope of the curve, as illustrated in Fig. 8. The k_{app} value continuously increased as the C-doping concentration increased, with x = 0, k_{app} = 0.0091 min^{-1}, x = 0.05, k_{app} = 0.01032 min^{-1}, x = 0.1, k_{app} = 0.01466 min^{-1}, x = 0.2, and k_{app} = 0.01273 min^{-1}. The C-doped CeO_2 nanoparticles with a carbon concentration of 10 mol% exhibitted the highest k_{app} of 0.01466 min^{-1}, which was much higher than that of the undoped CeO_2 nanoparticles.

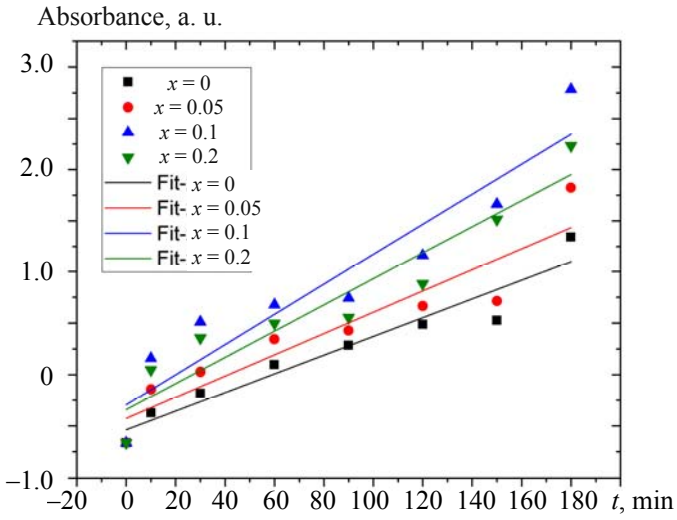

Fig. 8. MB degradation performance of the $Ce_{1-x}C_xO_2$ nanoparticles, x = 0–0.2.

The C-doped CeO_2 nanoparticle has more defects than the undoped CeO_2 nanoparticle, thereby increasing the number of oxygen vacancies. The oxygen diffusion rate in the crystal lattice is increased, preventing the recombination of electron and hole pairs, thereby increasing the photocatalytic activity.

The present reaction occurred through the following mechanism. The first reaction is due to $h\nu$ radiation, creating electron-hole pairs, combining with water to form hydroxyl radical species (•OH), and then oxidizing MB to CO_2, H_2O, and N_2 as illustrated below:

$$CeO_2 + h\nu \rightarrow CeO_2\ (\text{hole}) + \text{electron}$$
$$\text{Hole} + H_2O \rightarrow \bullet OH$$
$$\text{Electron} + O_2 \rightarrow \bullet O_2^-$$
$$H_2O + \bullet O_2^- \rightarrow \bullet OH + OH^- + O_2$$
$$\bullet OH + \bullet O_2^- + \text{hole} + MB \rightarrow CO_2 + H_2O + N_2$$

Conclusions. We have demonstrated the nanostructure and enhanced visible light photodegradation activity of MB in the presence of the C-doped CeO_2 nanoparticles. The grain size of the CeO_2 crystals can be adjusted by varying the carbon concentration. The degradation rate of MB increased in the C-doped CeO_2 nanoparticles. The reason for the improved photocatalyst activity was that the C-doped CeO_2 nanoparticles reduced the recombination of the electron-hole pair. These findings suggest that the present method is useful for controlling the microstructure and the dye degradation properties of the C-doped CeO_2 nanoparticles, which is particularly important for catalyst engineering.

Acknowledgments. This research is funded by the Hanoi University of Science and Technology (HUST) under project number T2021-PC-024.

REFERENCES

1. P. T. Lum, K. Y. Foo, N. A. Zakaria, P. Palaniandy, *Mater. Chem. Phys*., **241**, 122405 (2020).
2. N. Y. Donkadokula, A. K. Kola, I. Naz, D. Saroj, *Rev. Environ. Sci. Biotechnol*., **19**, 543–560 (2020).
3. U. G. Akpan, B. H. Hameed, *J. Hazard Mater*., **170**, 520–529 (2009).
4. P. V. Huan, P. D. Tam, V. H. Pham, *J. Electron. Mater*., **48**, 5294–5300 (2019).
5. R. Ma, S. Zhang, T. Wen, P. Gu, L. Li, G. Zhao, et al., *Catal. Today,* **335**, 20–30 (2019).
6. J. Fu, J. Yu, C. Jiang, B. Cheng, *Adv. Energy Mater*., **8**, 1701503 (2018).
7. C. Sun, H. Li, L. Chen, *Energy Environ. Sci*., **5**, 8475–8505 (2012).
8. L. Liu, Y. Pu, Y. Lu, N. Li, Z. Hu, S. Chen, *J. Membr. Sci*., **621**, 118972 (2021).
9. G. E. Malashkevich, V. B. Prokopenko, D. V. Dem'yanenko, I. M. Mel'nichenko, *Phys. Solid State*, **41**, 1815–1820 (1999).

10. A. A. Fauzi, A. A. Jalil, N. S. Hassan, F. F. A. Aziz, M. S. Azami, I. Hussain, et al., *Chemosphere,* **286**, 131651 (2022).
11. D. Channei, B. Inceesungvorn, N. Wetchakun, S. Ukritnukun, A. Nattestad, J. Chen, et al., *Sci. Rep.,* **4**, 5757 (2014).
12. N. S. Arul, D. Mangalaraj, P. C. Chen, N. Ponpandian, P. Meena, Y. Masuda, *J. Sol-Gel Sci. Technol*., **64**, 515–523 (2012).
13. A. Akbari-Fakhrabadi, R. Saravanan, M. Jamshidijam, R. V. Mangalaraja, M. A. Gracia, *J. Saudi Chem. Soc*., **19**, 505–510 (2015).
14. N. Kovalevskiy, D. Selishchev, D. Svintsitskiy, S. Selishcheva, A. Berezin, D. Kozlov, *Catal. Commun*., **134**, 105841 (2020).
15. H. Wang, J. P. Lewis, *J. Phys.: Cond. Matter*., **17**, L209 (2005).
16. J. S. Lee, S. C. Choi, *Mater. Lett*., **58**, 390–393 (2004).
17. M. Hirano, E. Kato, *J. Am. Ceram. Soc*.,**79**, 777–780 (1996).
18. A. Khorsand Zak, W. H. Abd. Majid, M. E. Abrishami, R. Yousefi, *Solid State Sci*., **13**, 251–256 (2011).
19. P. V. Huan, B. T. Hue, B. T. Hoan, N. T. H. Hanh, H. N. Van, C. X. Thang, et al., *Mater. Sci. Eng. B,* **262**, 114794 (2020).
20. S. Patil, A. Sandberg, E. Heckert, W. Self, S. Seal, *Biomaterials*, **28**, 4600–4607 (2007).
21. F. Zhang, Q. Jin, S. W. Chan, *J. Appl. Phys*., **95**, 4319 (2004).
22. T. Ravishankar, T. Ramakrishnappa, G. Nagaraju, H. Rajanaika, *Chem. Open*, **4**, 146–154 (2015).
23. R. Zamiri, H. A. Ahangar, A. Kaushal, A. Zakaria, G. Zamiri, D. Tobaldi, et al., *PLoS One,* **10**, e0122989 (2015).
24. T. Mokkelbost, I. Kaus, T. Grande, M. A. Einarsrud, *Chem. Mater*., **16**, 5489–5494 (2004).
25. H. Ming, Z. Ma, Y. Liu, K. Pan, H. Yu, F. Wang, et al., *Dalton Transact.,* **41**, 9526–9531 (2012).
26. J. Tauc, R. Grigorovici, A. Vancu, *Phys. Status Solidi* (*b*), **15**, 627–637 (1966).